

Microstructure and mechanical properties of additively manufactured Inconel 718: A comparative study between L-PBF and LP-DED

Nabeel Ahmad^{1,2}, Shaharyar Baig^{1,2}, Reza Ghiaasiaan^{1,2}, Paul R. Gradl³, Shuai
Shao^{1,2}, Nima Shamsaei^{1,2*}

¹National Center for Additive Manufacturing Excellence (NCAME), Auburn
University, Auburn, AL 36849, USA

²Department of Mechanical Engineering, Auburn University, Auburn, AL36849,
USA

³NASA Marshall Space Flight Center, Propulsion Department, Huntsville, AL
35812, USA

*Corresponding author:

Email: shamsaei@auburn.edu

Phone: (334) 844 4839

Abstract

This study aims to characterize the microstructure and mechanical properties of Inconel 718 fabricated using two different additive manufacturing processes: laser powder bed fusion (L-PBF) and laser powder directed energy deposition (LP-DED). Similar heat treatments (HTs) including stress-relief (1065°C for 1.5 hr), hot isostatic pressing (1162°C under 100 MPa isostatic pressure of Ar gas for 3 hr), solution annealing (1065°C for 1 hr), and two-step ageing (760°C for 10 hr + 650°C for 10 hr) are applied to both batches. Scanning electron microscopy is utilized to characterize microstructural evolution during each step of HTs for both samples. Tensile tests are performed to evaluate the mechanical properties at room temperature. Elongation to failure of L-PBF specimens is measured to be 16% lower than that of the LP-DED ones, while the ultimate tensile and yield strengths of L-PBF specimens are, respectively, 9% and 6% higher, compared to the LP-DED ones. The differences in tensile properties between two specimens are explained using microstructural and fracture surfaces analysis.

Keywords: Additive manufacturing, laser powder bed fusion (L-PBF), laser powder directed energy deposition (LP-DED), Inconel 718, grain size, tensile properties

Introduction

Additive manufacturing (AM) has gained popularity because of its capabilities to fabricate complex geometries as well as difficult-to-machine alloys [1], such as Inconel 718 (IN718). IN718 is primarily a γ' -strengthened nickel-based superalloy, which is intended for high temperature applications. Due to its good weldability, IN718 has recently received significant attention from AM communities [2]. The layer-by-layer

nature of AM processes allows the fabrication of near-net-shaped components, which significantly reduces the need for post-processing [3].

Different AM technologies employ unique process parameters (i.e., power, scan speed, layer thickness, etc.), leading to different characteristics in their final products [4]. For instance, laser powder directed energy deposition (LP-DED) employs higher laser powers and layer thicknesses than laser powder bed fusion (L-PBF) process and is typically used to build large volumes, while L-PBF is used for components requiring higher geometrical resolution [4]. Solidification/cooling rate of LP-DED specimens is typically lower than that of L-PBF ones [5,6]. Such differences in cooling rates can significantly influence microstructure and subsequently mechanical properties in L-PBF and LP-DED components [5,6].

The objective of this study is to examine the effect of the standard heat treatment (HT) schedule on the microstructural and mechanical properties of L-PBF and LP-DED IN718 specimens. This article is presented in the following sequence: first, the experimental procedure is explained, including the materials, fabrication, and testing methodology; then the experimental results are presented, discussed, and compared with existing data in the literature and finally, conclusions are presented.

Experimental Procedure

The chemical compositions of the two powder batches used for fabrication are presented in **Table 1**. Cylindrical bars of IN718 were manufactured vertically using L-PBF and LP-DED technologies. The process parameters used for fabrication are tabulated in **Table 2**. The original bars of both specimens were cut from the build plate using wire electron discharge machining to reduce the risk of geometrical distortion, upon which they were heat treated (HT) according to standard multi-step HT schedules shown schematically in **Figure 1**. Stress relief (SR, 1065°C for 1.5 hr) and hot isostatic pressing (HIP, 1162 °C under 100 MPa isostatic pressure of Ar for 3 hr) were performed following ASTM F3055 [8] and ASTM F3301 [9] standards, respectively, while solution annealing (SOL, 1065 °C for 1 hr) and 2-step aging (AGE, 760°C for 10 hr + 650 °C for 10 hr) were carried out according to AMS 5664 [10] standard. Upon HT, the bars were machined to the final geometry of tensile test specimen (see **Figure 2**) according to ASTM E8 standard [7].

Microstructural evolution during the HT processes was studied using small samples cut from the tensile specimens in the radial plane (i.e., perpendicular to the build direction). The metallography procedure of microstructural samples was conducted according to ASTM-E3 [11] standard in the following order: cold-mounted, ground using SiC sandpapers with grit sizes ranging from 200 to 1200, and finally polished using 0.05 micron colloidal silica suspension. For the electron backscatter diffraction (EBSD) analysis, an extra vibratory polishing step using 0.02 micron colloidal silica suspension was also included to remove residual stresses induced during the grinding stage. Microstructural analysis was performed using a Zeiss crossbeam 550 scanning electron microscope (SEM) equipped with EBSD and energy

dispersive spectroscopy (EDS) detectors. Backscattered electron (BSE) imaging was obtained using electron contrast channeling imaging (ECCI) [12].

Tensile tests were conducted following ASTM E8 [7] standard using a strain rate of 0.005 mm/mm/min. During tensile testing, an extensometer was attached to the specimen until failure to record strain values. A 0.2% offset method was used to calculate yield strength. Upon failure, tensile fracture surfaces were ultrasonically cleaned to eliminate contaminants as preparation for fractography using SEM.

Table 1. Chemical composition of powders used for fabrication of L-PBF and LP-DED IN718 specimens.

Elements	L-PBF IN718	LP-DED IN718
	Wt.%	Wt.%
C	0.03	0.04
Mn	0.08	0.11
Si	0.09	0.06
S	<0.015	<0.001
P	0.01	0.01
Cr	18.09	18.81
Fe	18.33	Bal
Co	0.35	<0.1
Mo	2.91	3.01
Nb+Ta	5.00	5.18
Ti	0.95	0.96
Al	0.38	0.52
B	<0.006	0.00
Cu	0.04	0.02
Ca	<0.01	-??
O	0.01	0.01
N	0.03	<0.001
Se	<0.005	??
Ni	53.60	52.69

Table 2. Process parameters used in this study to fabricate L-PBF and LP-DED IN718 specimens.

Process	Power (W)	Layer thickness (µm)	Travel speed (mm/min)	Powder feed rate (g/min)
L-PBF	285	40	57,600	---
LP-DED	1070	381	1016	16

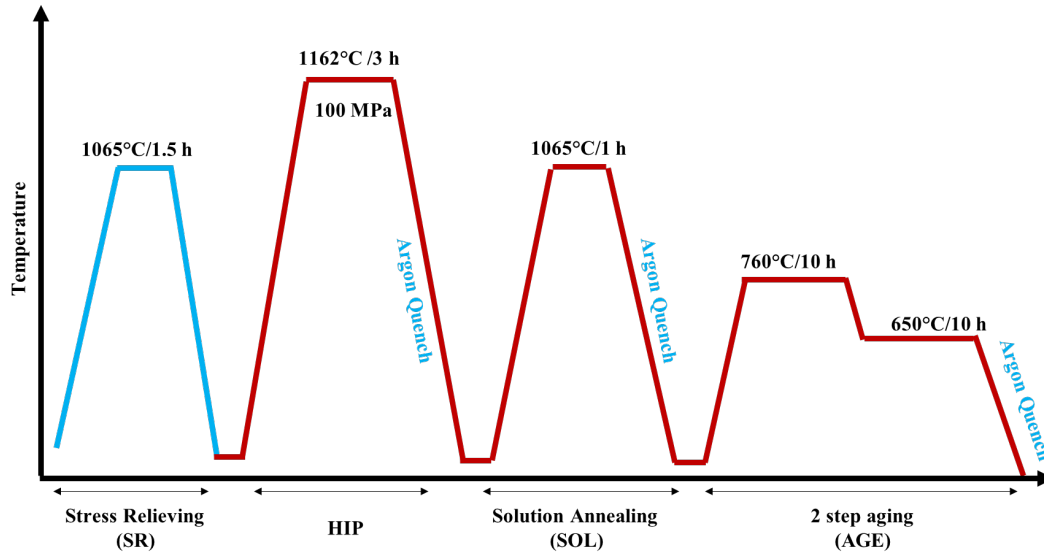


Figure 1. Schematic presentation of multi-step standard HT schedule used for this study for both L-PBF and LP-DED IN718 specimens.

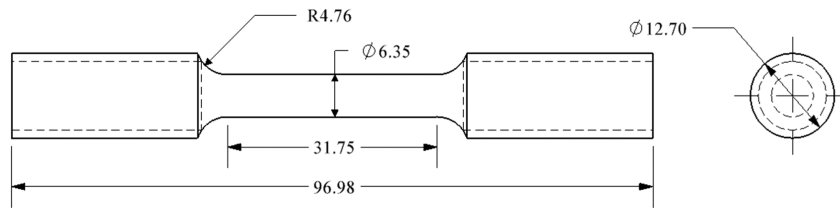


Figure 2. Geometry of threaded tensile test specimens used in this study according to ASTM E8 [7] standard. All the dimensions are in mm.

Results and Discussion

Inverse pole figure (IPF) maps obtained from EBSD analysis on the radial plane of L-PBF and LP-DED IN718 samples are shown in the **Figure 3** for different HT steps such as non-heat treated (NHT), SR, SR+HIP, SR+HIP+SOL, and SR+HIP+SOL+AGE. The average grain size of L-PBF IN718 samples was smaller than LP-DED samples for each corresponding steps of HT even though similar HT procedures were followed. The average grain size in the NHT microstructure of L-PBF and LP-DED was ~16- and ~26- μm , respectively. The finer grain structure of L-PBF specimens is attributed to the higher cooling rates of L-PBF process [5]. Following SR, no change in grain size was seen. After HIP at 1162°C, considerable grain growth occurred, and several annealing twins occupied the microstructures of both LP-DED and L-PBF samples. Such grain growth after HIP has also been seen in literature [13,14] and is associated with higher HIP temperature (~1162°C), assisting grain growth. Note that the effect of HIP on grain growth in LP-DED samples is more pronounced than that of L-PBF ones, signifying that the microstructural response of AM IN718 to the applied HT routine differs depending on the initial grain structure.

After SOL and AGE, there was no change in grain size in both L-PBF and LP-DED samples.

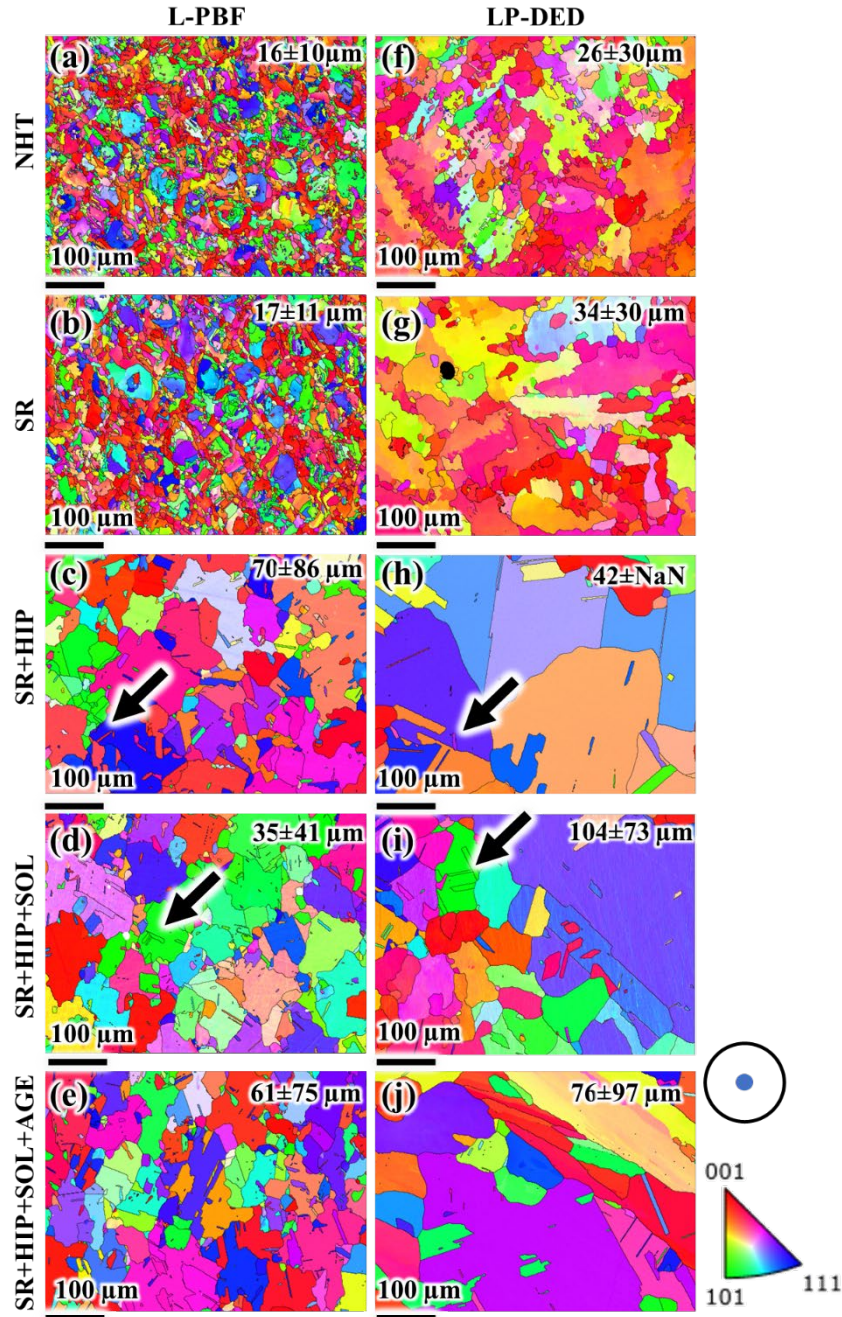


Figure 3. IPF maps obtained from EBSD analysis on the radial plane of L-PBF and LP-DED IN718 specimens during different HT steps including NHT in (a)-(f), SR in (b)-(g), SR+HIP in (c)-(h), SR+HIP+SOL in (d)-(i), SR+HIP+SOL+AGE in (i)-(j), respectively. Black arrows point at annealing twins.

BSE micrographs taken in the radial plane are shown in **Figure 4**. NHT samples for both LP-DED and L-PBF IN718 consisted of a dendritic microstructure and had severe micro-segregations of alloying elements (indicated using yellow arrows in

Figures 4(a)-(f) due to the fast cooling rates during fabrication process [15]. Bright bulky phases as shown in **Figures 4(a)-(f)** were characterized using EDS analysis (see **Figure 5**) which revealed that these particles were rich in Nb and Mo but poor in Cr, Fe, and Ni and were characterized as Laves phase [16]. It should be noted that the Laves phases (bright phases) seem to be larger in size (~2 micron) in LP-DED samples. Upon further HTs starting from SR (see **Figures 4(b) and (g)** for L-PBF and LP-DED specimens, respectively), the micro-segregations of alloying elements started to dissolve into γ -matrix as supersaturated solid solution, while the metal carbide phases, i.e., Mo-rich (M_6C) and Cr-rich ($M_{23}C_6$) carbides [17], were formed at both grain boundaries (GBs) and inside grains (see EDS analysis in **Figure 6**). As shown in **Figures 4(c)-(e) and (g)-(j)**, after HIP, the dendritic microstructure and the micro-segregation are almost completely removed in both specimens.

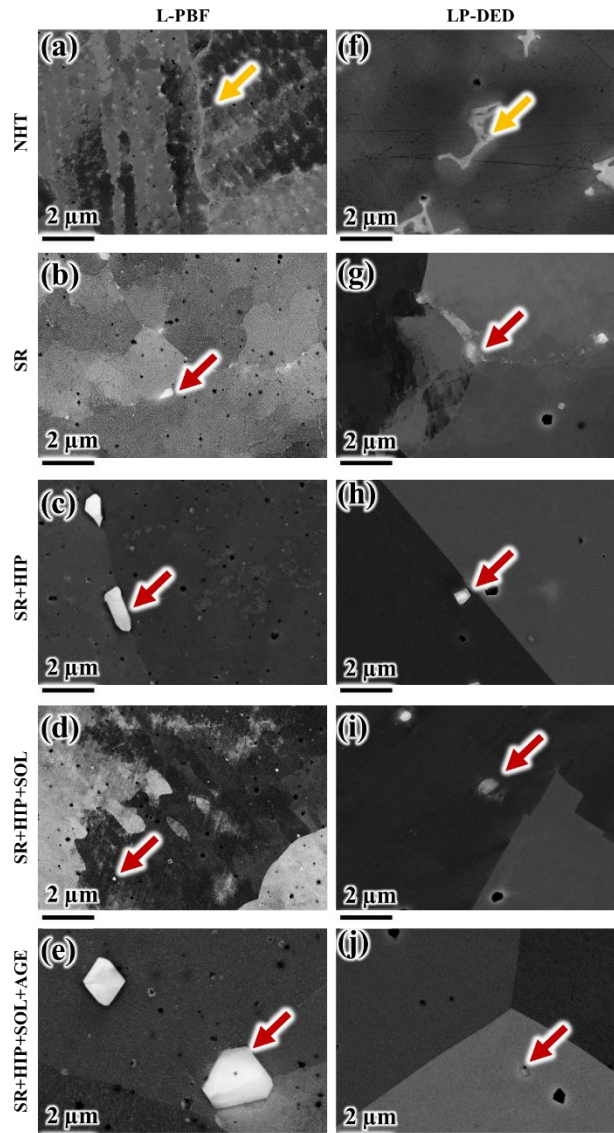


Figure 4. BSE micrographs obtained using ECCI technique on the radial plane, i.e., perpendicular to build direction, of L-PBF and LP-DED IN718 specimens during different HT steps including NHT in (a)-(f), SR in (b)-(g), SR+HIP in (c)-(h),

SR+HIP+SOL in (d)-(i), SR+HIP+SOL+AGE in (e)-(j), respectively. Note that yellow arrows are pointing at Laves, and red arrows are showing metal carbide particles.

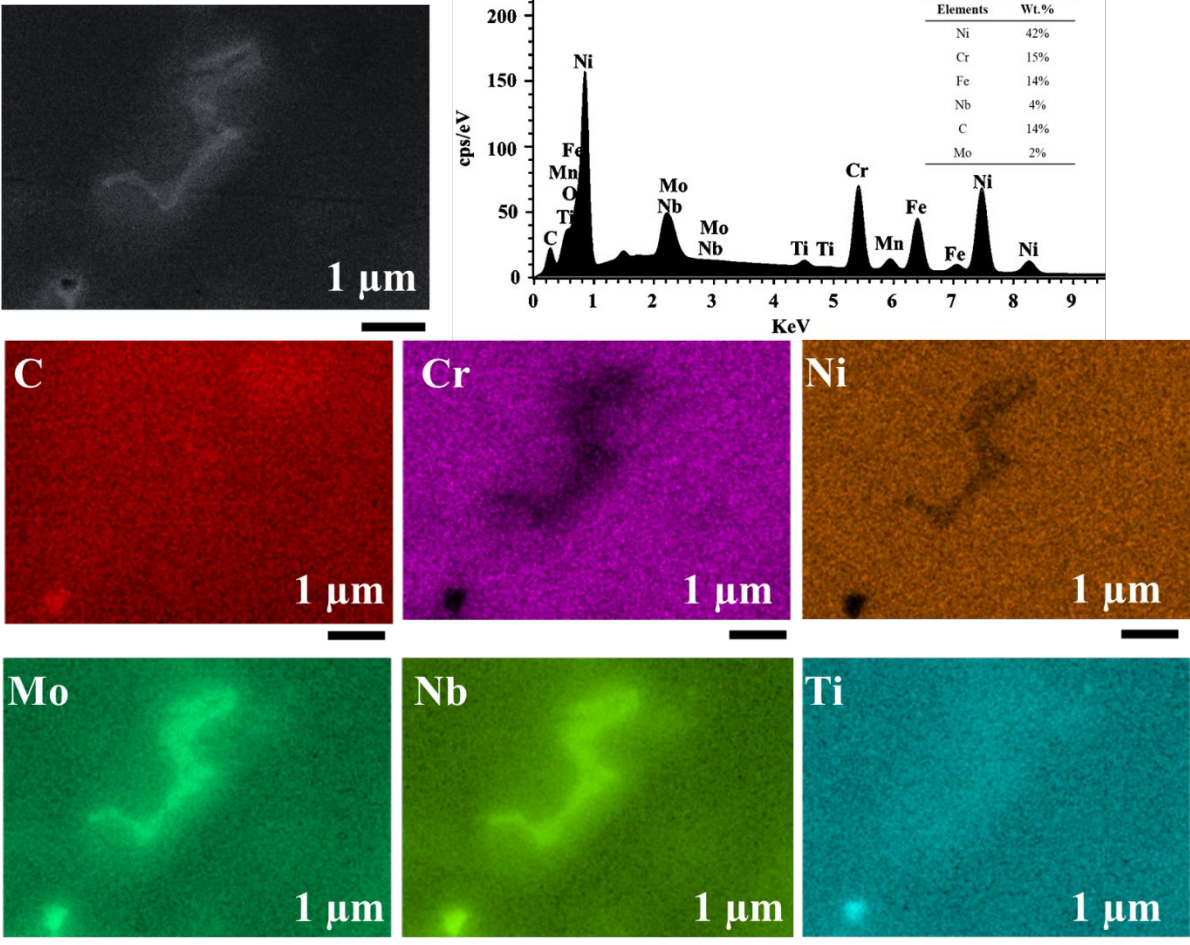


Figure 5. Elemental maps obtained from EDS analysis for a NHT LP-DED IN718 sample.

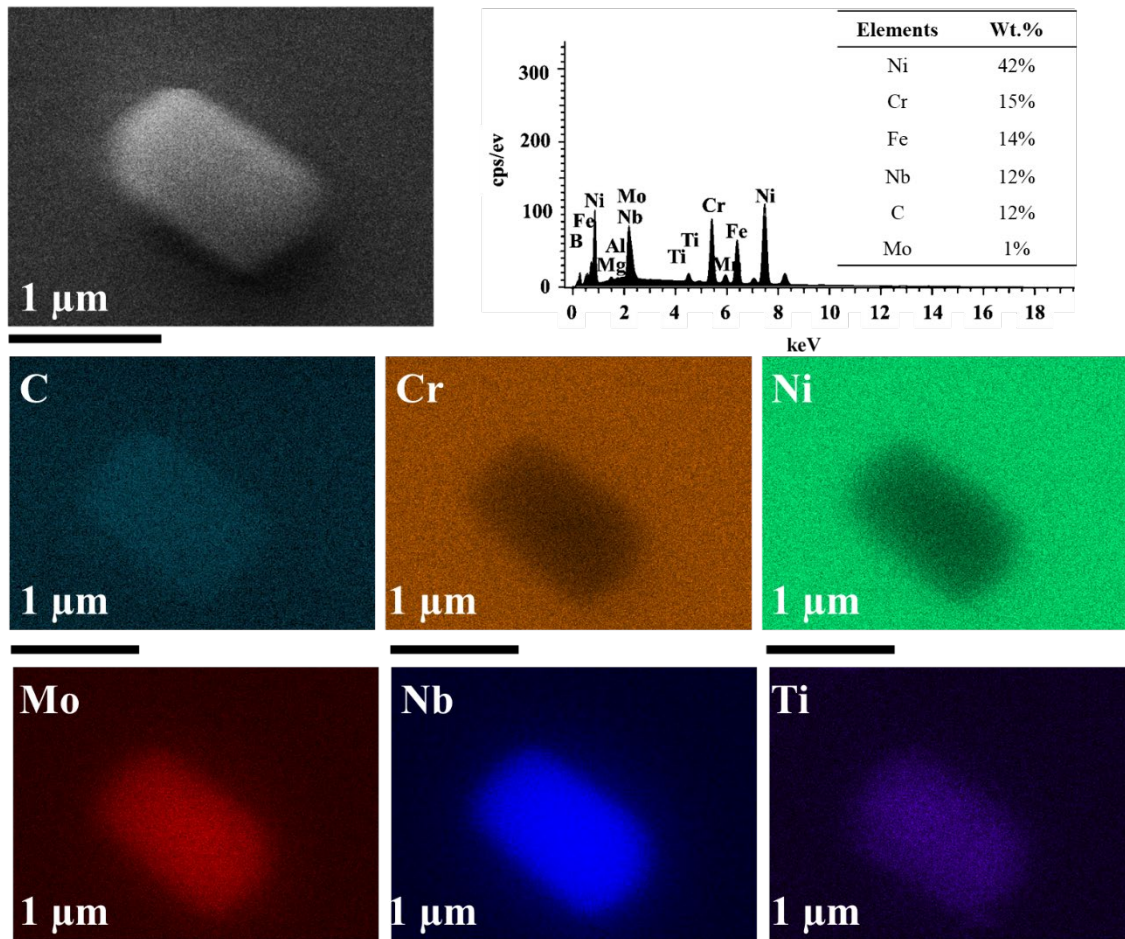


Figure 6. Elemental maps obtained from EDS analysis for a fully HT L-PBF IN718 sample showing a Mo and Nb rich carbides.

Engineering stress-strain curves of LP-DED and L-PBF IN718 specimens in fully HT conditions are presented in **Figure 7(a)**. Furthermore, **Figure 7(b)** presents the tensile properties (i.e., highlighted ultimate tensile strength (UTS), yield strength (YS), and elongation to failure (EL)) of both specimens are compared with those of other IN718 specimens obtained from literature such as L-PBF [18,19], electron powder bed fusion (E-PBF) [20] and wrought [21,22] counterparts. As shown in **Figure 7(a)**, L-PBF IN718 specimens possessed ~9% and 6% higher UTS and YS, respectively, than LP-DED IN718 specimens, which can be attributed to the finer grain structure in the former (see **Figure 3**). Furthermore, it can be seen in **Figure 7(b)** that L-PBF IN718 specimens have ~16% lower EL than LP-DED IN718 ones, which could be attributed to the relatively large carbide phases observed in the former (compare **Figure 4(e)** vs. **(j)**). Interface debonding at larger carbides lead to larger microvoids, which can result in early fracture [23]. It is also notable in **Figure 7(b)** that the L-PBF and LP-DED IN718 specimens showed similar tensile properties with their AM and wrought counterparts. Fracture surfaces of both LP-DED and L-PBF IN718 specimens are presented in the **Figure 8**. Both fracture surfaces consisted of central flat region and a shear lip regions. Higher magnification images taken from the central regions

showed several dimples, indicative of ductile fracture. The size of dimples in L-PBF specimens were slightly finer than LP-DED ones, which correlated well with the carbide size and EL of former.

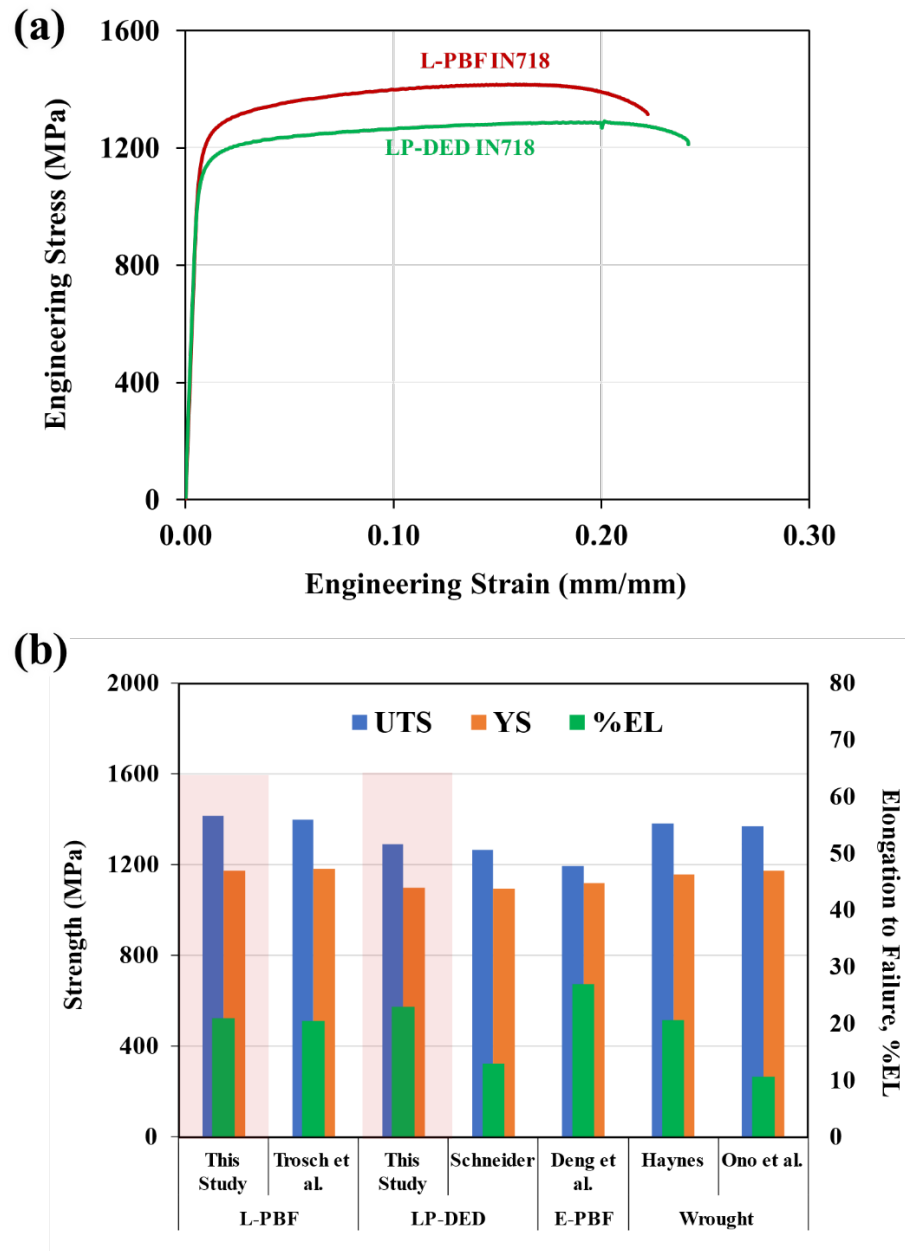


Figure 7. Tensile behavior of LP-DED and L-PBF IN718 specimens: (a) engineering stress-strain curves (b) bar charts for tensile properties such as UTS, YS, and EL are compared with L-PBF [17,18], E-PBF [19], and wrought [20,21] counterparts.

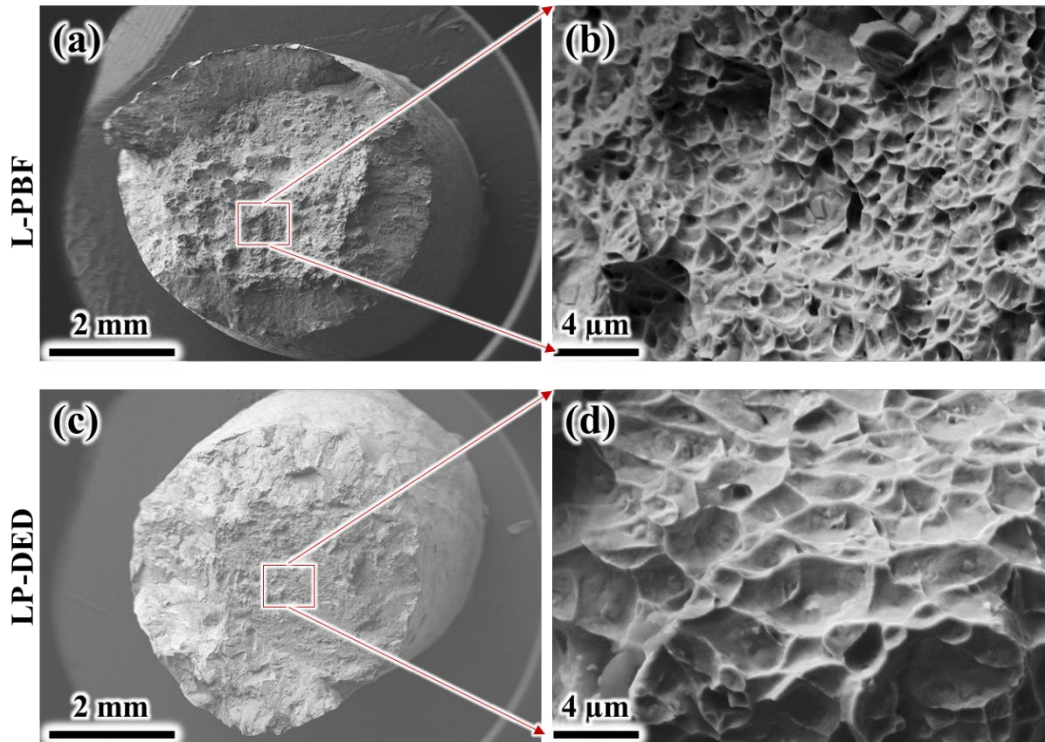


Figure 8. Tensile fracture surfaces for L-PBF IN718 specimens in (a)-(b) and LP-DED IN718 ones in (c)-(d), respectively.

Conclusions

In this study, the effect of heat treatment (HT) was investigated on the microstructure and mechanical properties of IN718 fabricated using two different processes, namely, laser powder bed fusion (L-PBF) and laser powder directed energy (LP-DED). The following conclusions can be drawn from the experimental observations:

- 1) The non-heat treated (NHT) microstructures of L-PBF and LP-DED specimens showed fine dendritic microstructures with severe micro-segregation of alloying elements.
- 2) L-PBF IN718 alloy exhibited a finer grain structure as compared to LP-DED IN718 samples which could be attributed to the higher solidification rate during fabrication in the former.
- 3) Upon full HT, the prior dendritic microstructure with severe micro-segregation observed in NHT conditions were all dissolved in the γ -matrix while Mo-rich (M_6C) carbides were formed at grain boundaries and inside grains for both specimens.
- 4) L-PBF IN718 specimens in fully HT exhibited slightly better tensile strengths than those of LP-DED IN718 ones which were ascribed to the finer grain structure observed in the former.
- 5) L-PBF IN718 specimens showed lower elongation to failure compared to LP-DED IN718 ones, which could be attributed to the relatively large carbide phases that yielded larger microvoids, and lead to early fracture. Finer dimples in L-PBF specimens than LP-DED ones further validated this observation.

Acknowledgment

This research is partially supported by the National Aeronautics and Space Administration (NASA) under Cooperative Agreement No. 80MSFC19C0010. This paper describes objective technical results and analysis. Any subjective views or opinions that might be expressed in the paper do not necessarily represent the views of the NASA or the United States Government.

References

- [1] Yadollahi A, Shamsaei N. Additive manufacturing of fatigue resistant materials: Challenges and opportunities. *Int J Fatigue* 2017;98:14–31. <https://doi.org/10.1016/j.ijfatigue.2017.01.001>.
- [2] Hosseini E, Popovich VA. A review of mechanical properties of additively manufactured Inconel 718. *Addit Manuf* 2019;30:100877. <https://doi.org/10.1016/j.addma.2019.100877>.
- [3] Lee S, Ahmad N, Corriveau K, Himel C, Silva DF, Shamsaei N. Bending properties of additively manufactured commercially pure titanium (CPTi) limited contact dynamic compression plate (LC-DCP) constructs: Effect of surface treatment. *J Mech Behav Biomed Mater* 2022;126:105042. <https://doi.org/10.1016/j.jmbbm.2021.105042>.
- [4] DebRoy T, Wei HL, Zuback JS, Mukherjee T, Elmer JW, Milewski JO, et al. Additive manufacturing of metallic components – Process, structure and properties. *Prog Mater Sci* 2018;92:112–224. <https://doi.org/10.1016/j.pmatsci.2017.10.001>.
- [5] Babuska TF, Krick BA, Susan DF, Kustas AB. Comparison of powder bed fusion and directed energy deposition for tailoring mechanical properties of traditionally brittle alloys. *Manuf Lett* 2021;28:30–4. <https://doi.org/10.1016/j.mfglet.2021.02.003>.
- [6] Nezhadfar PD, Gradl PR, Shao S, Shamsaei N. Microstructure and Deformation Behavior of Additively Manufactured 17–4 Stainless Steel: Laser Powder Bed Fusion vs. Laser Powder Directed Energy Deposition. *Jom* 2022;74:1136–48. <https://doi.org/10.1007/s11837-021-05032-y>.
- [7] F3056-14e1. Standard Specification for Additive Manufacturing Nickel Alloy (UNS N07718) with Powder Bed Fusion. 2014. <https://doi.org/10.1520/F3055-14A>. Copyright.
- [8] ASTM F3301. Standard for Additive Manufacturing – Post Processing Methods – Standard Specification for Thermal Post-Processing Metal Parts Made Via Powder Bed Fusion. *ASTM Stand* 2018;3. <https://doi.org/10.1520/F3301-18A.2>.
- [9] SAE International. AMS5664F: Nickel Alloy, Corrosion and Heat Resistant, Bars, Forgings, and Rings, 52.5Ni - 19Cr - 3.0Mo - 5.1Cb - 0.90Ti - 0.50Al - 18Fe, Consumable Electrode or Vacuum Induction Melted 1950 °F (1066 °C) Solution Heat Treated, Precipitation Hardenable - SA. 2017.
- [10] Committee, E08 AE. Standard Test Methods for Tension Testing of Metallic Materials. *ASTM International*; 2020.
- [11] ASTM E3. Standard Guide for Preparation of Metallographic Specimens Standard Guide for Preparation of Metallographic Specimens 1. vol. 03.01. 2012. <https://doi.org/10.1520/E0003-11R17.1>.
- [12] Zaefferer S, Elhami N-N. Theory and application of electron channelling contrast imaging under controlled diffraction conditions. *Acta Mater* 2014;75:20–50. <https://doi.org/10.1016/j.actamat.2014.04.018>.
- [13] Blackwell PL. The mechanical and microstructural characteristics of laser-deposited IN718. *J Mater Process Technol* 2005;170:240–6. <https://doi.org/10.1016/j.jmatprotec.2005.05.005>.
- [14] Ghiaasiaan R, Poudel A, Ahmad N, Gradl PR, Shao S, Shamsaei N. High Temperature Tensile and Fatigue Behaviors of Additively Manufactured IN625 and IN718. *Procedia Struct Integr* 2022;38:581–7. <https://doi.org/10.1016/j.prostr.2022.03.059>.

- [15] Fayed EM, Shahriari D, Saadati M, Brailovski V, Jahazi M, Medraj M. Influence of homogenization and solution treatments time on the microstructure and hardness of Inconel 718 fabricated by laser powder bed fusion process. *Materials (Basel)* 2020;13:1–17. <https://doi.org/10.3390/ma13112574>.
- [16] Gallmeyer TG, Moorthy S, Kappes BB, Mills MJ, Amin-Ahmadi B, Stebner AP. Knowledge of process-structure-property relationships to engineer better heat treatments for laser powder bed fusion additive manufactured Inconel 718. *Addit Manuf* 2020;31:100977. <https://doi.org/10.1016/j.addma.2019.100977>.
- [17] Ghiaasiaan R, Poudel A, Ahmad N, Muhammad M, Gradl PR, Shao S, et al. Room Temperature Mechanical Properties of Additively Manufactured Ni-base Superalloys: A Comparative Study. *Procedia Struct Integr* 2022;38:109–15. <https://doi.org/10.1016/j.prostr.2022.03.012>.
- [18] Schneider J. Comparison of Microstructural Response to Heat Treatment of Inconel 718 Prepared by Three Different Metal Additive Manufacturing Processes. *JOM* 2020;72:1085–91. <https://doi.org/10.1007/s11837-020-04021-x>.
- [19] Trosch T, Strößner J, Völkl R, Glatzel U. Microstructure and mechanical properties of selective laser melted Inconel 718 compared to forging and casting. *Mater Lett* 2016;164:428–31. <https://doi.org/10.1016/j.matlet.2015.10.136>.
- [20] Deng D. Additively Manufactured Inconel 718 : Microstructures and Mechanical Properties. 2018.
- [21] International H. HAYNES® 718 alloy. 2020.
- [22] Ono Y, Yuri T, Sumiyoshi H, Takeuchi E, Matsuoka S, Ogata T. High-cycle fatigue properties at cryogenic temperatures in INCONEL 718. *AIP Conf Proc* 2006;824 l:184–91. <https://doi.org/10.1063/1.2192350>.
- [23] Ahmad N, Ghiaasiaan R, Gradl PR, Shao S, Shamsaei N. Revealing deformation mechanisms in additively manufactured Alloy 718: Cryogenic to elevated temperatures. *Mater Sci Eng A* 2022;849:143528. <https://doi.org/10.1016/j.msea.2022.143528>.